Appl. Phys. B 68, 777–784 (1999) / DOI 10.1007/s003409901499

Applied Physics B
Lasers
and Optics

Photorefractive properties of highly-doped lithium niobate crystals in the visible and near-infrared

K. Peithmann, A. Wiebrock, K. Buse

Fachbereich Physik, Universität Osnabrück, D-49069 Osnabrück, Germany

Received: 18 November 1998/Revised version: 8 January 1999/Published online: 7 April 1999

Abstract. Light-induced refractive-index changes, bulk-photovoltaic current densities, and photoconductivities of photorefractive iron-doped lithium niobate crystals (iron concentrations between 0.02 and 0.17 wt. %) are investigated in detail using visible and near-infrared light. It turns out that the one-center model predicts the material performance correctly for small iron concentrations ($c_{\mathrm{Fe}} < 0.06$ wt. % Fe_2O_3), only. A strong increase of the photoconductivity for higher doping levels limits the space-charge fields. Refractive-index changes up to 7×10^{-4} for green and 2.8×10^{-4} for near-infrared ordinarily polarized light are obtained. The corresponding hologram multiplexing numbers are 11 for green and 5 for near-infrared light.

PACS: 42.65; 42.70; 72.40; 78.20

The photorefractive effect was discovered in lithium niobate crystals ($LiNbO_3$) by Ashkin et al. in 1966 [1]. Chen et al. recognized only two years later that these crystals are useful for holographic recording [2]. Chen also pointed out that inhomogeneous illumination builds up space-charge fields which modulate the refractive index via the electro-optic effect. Although since these early days many other electro-optic crystals are found to be also photorefractive, lithium niobate is still the best choice for many applications, such as reversible holographic data storage [3–6], outstanding interference filtering [7, 8], or wavelength division multiplexing [9].

The origin of the light-induced space-charge fields was elucidated in the seventies. It was discovered that transition metal impurities play an important role [10, 11] and that thermal annealing also has influence on the light-induced refractive-index changes [10, 11]. A publication by Glass et al. answered the question of the driving force responsible for build-up of the space-charge fields [12]: Bulk photovoltaic currents are present in $LiNbO_3$ upon illumination, and fields up to 100 kV/cm can be created. Absorption measurements, electron-paramagnetic resonance, and Mössbauer spectroscopy revealed that iron ions occur in $LiNbO_3$ only in two different valence states, Fe^{2+} and Fe^{3+} [13]. Quantitative measurements of the concentrations of these ions [13, 14] enabled further progress. The bulk photovoltaic current density j_{phv} was found to be proportional to the concentration $c_{Fe^{2+}}$ of Fe^{2+} ions [15, 16], the photoconductivity σ_{ph} increases linearly with the ratio $c_{Fe^{2+}}/c_{Fe^{3+}}$ of Fe^{2+} and Fe^{3+} ions [16–18], and the saturation values of the refractive-index changes Δn_{s} depend on $c_{Fe^{3+}}$ [19]. Krätzig and co-workers established by this and further work the Fe^{2+}/Fe^{3+} one-center charge-transport model for $LiNbO_3$ [16]. Electrons are excited from Fe^{2+} to the conduction band, they are moved by the bulk photovoltaic effect, diffusion and drift, and they are trapped elsewhere by Fe^{3+} ions. The one-center model serves since this time as the solid base for description of the light-induced charge transport in photorefractive crystals. Depending on the experimental conditions, on the dopants and on the host material used, extensions of the model might be necessary. Orlowski and Krätzig discovered that electrons and holes contribute simultaneously to the effects, if ultraviolet light is employed for recording in $LiNbO_3$ [20] and used for the first time beam-coupling [21] to reveal the sign of the dominating charge carriers [20]. Further extensions of the one-center model were developed later: Two-center and three-valence models [22, 23] describe the processes in, for example, $LiNbO_3$ at high light intensities (two-center system) [24] and in $KTa_{0.52}Nb_{0.48}O_3$ (KTN) in the continuous-wave regime (three-valence system) [25].

Sommerfeldt et al. checked and confirmed carefully the dependences $j_{\mathrm{phv}} \propto c_{Fe^{2+}}$, $\sigma_{\mathrm{ph}} \propto c_{Fe^{2+}}/c_{Fe^{3+}}$, and $\Delta n_{\mathrm{s}} \propto c_{Fe^{3+}}$ for $LiNbO_3$:Fe [26], but only crystals with iron concentrations up to $10 \times 10^{24}\,\mathrm{m}^{-3}$ (about 0.03 wt. % Fe_2O_3) were investigated. However, early work by Krätzig and Kurz indicates that these relations do not address the situation of highly doped material properly [27, 28]. Refractive-index changes increase only up to iron concentrations of $30 \times 10^{24}\,\mathrm{m}^{-3}$ (about 0.1 wt. % Fe_2O_3) and tend to decrease for higher iron contents.

Refractive-index changes as large as possible are desired for application of photorefractive $LiNbO_3$. Thus highly doped

Dedicated to Prof. Dr. Eckard Krätzig on the occasion of his 60th birthday.

crystals are of special interest. However, detailed information about Δn_s, j_{phv}, and σ_{ph} in these crystals is required in order to enable tailoring of crystal properties. We will describe in the next section the fundamentals of the one-center model and derive a simple formula for the dynamic range of $LiNbO_3$. The result will be analysed, especially with respect to the influence of the wavelength of the recording light. Experimental methods are presented in the next section, followed by the obtained experimental photorefractive, photovoltaic, and photoconductive data for $LiNbO_3$ crystals with up to $56 \times 10^{24}\,m^{-3}$ iron atoms (0.17 wt. % Fe_2O_3). The consequences of these results will be discussed.

1 Theoretical considerations

1.1 Space-charge field in terms of the one-center model

Sinusoidal light patterns are employed for theoretical and experimental investigation of photorefractive crystals. We may write for the light intensity

$$I(x) = I_0[1 + m\sin(Kx)]\,, \tag{1}$$

where x is a spatial coordinate, I_0 the averaged intensity, m the modulation degree, and K the spatial frequency.

Excitation of electrons from Fe^{2+} and recombination of conduction band electrons with Fe^{3+} are described by the rate equation

$$\frac{dN_e}{dt} = +(qSI + \beta)c_{Fe^{2+}} - rc_{Fe^{3+}}N_e\,, \tag{2}$$

where N_e is the concentration of conduction band electrons, q the quantum efficiency of excitation of an electron upon absorption of a photon, S the photon absorption cross section, β the thermal generation rate, and r the recombination coefficient. The steady-state condition yields

$$N_e = \frac{qSI + \beta}{r}\,\frac{c_{Fe^{2+}}}{c_{Fe^{3+}}}\,. \tag{3}$$

The conductivity σ consists of the photoconductivity σ_{ph} and the dark conductivity σ_{dark}. We may write $\sigma_{ph} = e\mu(qSI/r) \times (c_{Fe^{2+}}/c_{Fe^{3+}})$ and $\sigma_{dark} = e\mu(\beta/r)(c_{Fe^{2+}}/c_{Fe^{3+}})$, where e is the elementary charge and μ the charge-carrier mobility. Thermal excitations are negligible ($\beta \ll qSI$) if the photoconductivity exceeds the dark conductivity, which is typically the case for continuous wave illumination ($I \approx 10\,kW/m^2$) [29]. Considerable dark conduction can be taken into account, if necessary, by introduction of an effective modulation degree $m_{eff} = m\sigma_{ph}/(\sigma_{ph} + \sigma_{dark})$ of the pattern of conduction band electrons [30]. Anyhow, we will neglect thermal excitations in the following analysis, and the space-charge fields are always normalized to the modulation degree (E_{sc}/m for $m < 1$).

Drift currents $j_{drift} = \sigma_{ph}E_{sc}$, bulk photovoltaic currents

$$j_{phv} = \beta^* c_{Fe^{2+}} I\,, \tag{4}$$

and diffusion currents $j_{diff} = \mu k_B T(dN_e/dx)$ are the charge driving forces, where β^* is the bulk photovoltaic coefficient, k_B the Boltzmann constant, and T the temperature. Fourier development yields in the steady-state [31]

$$E_{sc} = -\left[\frac{E_{phv}^2 + E_D^2}{(1 + E_D/E_q)^2 + (E_{phv}/E_q')^2}\right]^{1/2}\,, \tag{5}$$

$$E_{phv} = \frac{j_{phv}}{\sigma_{ph}} = \frac{\beta^* r}{e\mu q S}c_{Fe^{3+}}\,, \quad E_D = \frac{k_B T}{e}K \tag{6}$$

$$E_q = \frac{e}{\epsilon\epsilon_0 K}\left(\frac{1}{c_{Fe^{2+}}} + \frac{1}{c_{Fe^{3+}}}\right)^{-1}\,, \tag{7}$$

$$E_q' = \frac{e}{\epsilon\epsilon_0 K}c_{Fe^{2+}}\,, \tag{8}$$

where E_{phv} is the photovoltaic field, E_D the diffusion field, and E_q and E_q' are space-charge limiting fields. Here ϵ is the dielectric coefficient and ϵ_0 is the permittivity of free space. Short-circuited conditions are assumed, i.e. the external electric field is zero.

The amplitude of the refractive-index grating for ordinarily polarized light is given by

$$\Delta n_s = -\frac{1}{2}n_o^3 r_{13}E_{sc}\,, \tag{9}$$

where n_o is the refractive index and r_{13} one of the electro-optic coefficients. Extraordinarily polarized light experiences larger refractive-index modulations, but is impractical for many applications: it cannot be employed for holographic storage in the 90° geometry because it would cause orthogonal polarization of the recording beams. Furthermore, extraordinary polarization assists holographic scattering to be built up [32], which has detrimental influence on storage applications. Telecommunication demands polarization-independent components, and devices made from $LiNbO_3$ suffer from birefringence. Thus geometries are selected where the light propagates almost along the optical axis, and only n_o and r_{13} are effective.

1.2 Dependencies

The following relations are valid considering (2)–(9):

$$\Delta n_s \propto c_{Fe^{3+}}\,, \tag{10}$$

$$j_{phv} \propto I\,c_{Fe^{2+}}\,, \tag{11}$$

$$\sigma_{ph} \propto I\,(c_{Fe^{2+}}/c_{Fe^{3+}})\,. \tag{12}$$

Dominant photovoltaic recording and negligible space-charge limiting fields are assumed ($E_{phv} \gg E_D$, $E_q \gg E_D$, $E_q' \gg E_{phv}$). These conditions are useful to elucidate the validity of the charge-transport model and to determine the underlying charge-transport parameters. However, the assumptions made above ($E_{phv} \gg E_D$, $E_q \gg E_D$, $E_q' \gg E_{phv}$) are not valid in the case of optimized material. We will perform in the following some simple estimations regarding tuning of $LiNbO_3$ for multiplexing of many holograms of high efficiency.

1.3 Dynamic range

Several holograms can be superimposed in the same volume. However, recording of new holograms partially erases all previously written ones. A measure for the multiplexing capability is the $M/\#$ [33]. It can be defined as follows:

$$\eta = \left(\frac{M/\#}{M}\right)^2 , \tag{13}$$

where η is the diffraction efficiency of each individual hologram (all of them are assumed to have the same diffraction efficiency) and M is the number of multiplexed holograms. An $M/\#$ of 1 indicates that 1000 holograms can be multiplexed, each of them with a diffraction efficiency of $\eta = 10^{-6}$. The $M/\#$ can be related to Δn via [33]:

$$M/\# = A_0 \frac{\tau_e}{\tau_r} , \tag{14}$$

$$A_0 = \frac{\pi \, \Delta n \, d}{\lambda \, \cos\Theta} \exp[-(\alpha d)/(2\cos\Theta)] , \tag{15}$$

where A_0 is the coupling coefficient, τ_r and τ_e are the time constants of recording and erasure, d is the thickness of the crystal, λ the vacuum wavelength of the recording light, Θ the half-angle between the recording beams inside the sample, and α the intensity absorption coefficient. The $M/\#$ quantifies the dynamic range of a recording material, and values of $M/\#$ as large as possible are desired.

1.4 Optimization of the dynamic range

Holograms are erased by recording of new ones. Thus recording and erasure take place simultaneously, and the light intensities for recording and erasure, which determine τ_r and τ_e, are the same. However, it is not evident that τ_r and τ_e are equal. The time constant for recording can be complex [34, 35], i.e. growth of the space-charge field is described by combination of a usual monoexponential function with a damped oscillation. At first glance, time constants of recording and erasure can become different in multiplexing experiments. This looks like an advantageous recording/erasure asymmetry. However, complex time constants originate from running holograms. Recording can become faster by this effect, and movement of holograms upon homogeneous erasure illumination does not increase the erasure speed. However, in practice holograms are erased by inhomogeneous recording illumination of new holograms. Different parts of the hologram move with different speeds according to the spatial variation of the light intensity. Acceleration of erasure is the consequence. There is no doubt, recording can become faster by complex time constants, but the erasure time constant decreases, too. Thus $\tau_r \approx \tau_e$ is a reasonable assumption which will be used in the following. This simplifies the equation for the $M/\#$ to $M/\# = A_0$.

Large values of $M/\#$ require large refractive-index modulations Δn. However, electrons are required to build up the space-charge fields. These electrons cause absorption, which decreases the $M/\#$. Proper selection of the concentrations $c_{Fe^{2+}}$ and $c_{Fe^{3+}}$ is required for optimization of the material. No absorption is caused by Fe^{3+} ions. The concentration $c_{Fe^{3+}}$ should be large enough to ensure

$$c_{Fe^{3+}} \gg c_{Fe^{2+}} , \tag{16}$$

$$c_{Fe^{3+}} \propto E_{phv} \gg E_D , \tag{17}$$

$$c_{Fe^{3+}} \propto E_{phv} \gg E'_q . \tag{18}$$

This avoids any kind of trap limitation and ensures dominant photovoltaic charge transport. Equations (5)–(8) simplify to

$$E_{sc} = -E'_q = -\frac{e}{\epsilon\epsilon_0 K} c_{Fe^{2+}} . \tag{19}$$

The space-charge field is limited by the density of electrons available for redistribution ($c_{Fe^{2+}}$). The intensity absorption coefficient α can be related to the concentration of Fe^{2+} centers via $\alpha = S c_{Fe^{2+}}$. Introduction of the abbreviation $\mathcal{A} = (S c_{Fe^{2+}} d)/(2\cos\Theta)$ yields

$$M/\# = \frac{\pi e n_0^3 r_{13}}{\epsilon\epsilon_0 \lambda K S} \mathcal{A} \exp(-\mathcal{A}) . \tag{20}$$

It turns out that the maximum $M/\#$ is

$$M/\# = \frac{\pi e}{\epsilon_0 \exp(1)} \frac{n_0^3 r_{13}}{\epsilon} \frac{1}{\lambda K} \frac{1}{S} . \tag{21}$$

To get this $M/\#$, a specific absorption is required: $\alpha = 2/d$. The factor 2 occurs because the absorption coefficient α is related to the intensity and not to the amplitude of the wave.

The first term on the right-hand side of (21) contains fundamental constants only. The second term consists of material parameters. However, this term is more or less equal for all known photorefractive materials, because materials with large r have also a large ϵ. The third term contains experimental parameters which are determined by geometry and laser used. The fourth parameter is a property of the filled electron traps; small photon excitation cross sections S are desired. Only this impurity parameter enters this final equation of the $M/\#$.

1.5 Quantitative estimations

Let us consider ordinarily polarized light of wavelength 514 nm. Parameters for $LiNbO_3$ are (room temperature): $n_0 = 2.33$ [36], $r_{13} = 12\,\mathrm{pm/V}$ [37, 38], $\epsilon = 28$ [39, 40], $K = (2\pi/0.15)\,\mu\mathrm{m}^{-1}$ (90° geometry) and $S = 4.6 \times 10^{-22}\,\mathrm{m}^2$ [13]. These parameters yield with (21) the result $M/\# = 11$.

The concentration $c_{Fe^{3+}}$ must be selected large enough to fulfill (16)–(18). The desired absorption is $100\,\mathrm{m}^{-1}$ for a 2-cm-thick crystal. With the S given above we get $c_{Fe^{2+}} = 0.22 \times 10^{24}\,\mathrm{m}^{-3}$. According to (16), the concentration $c_{Fe^{3+}}$ must be much larger. With the K given above and for room temperature we get $E_D = 1.1\,\mathrm{MV/m}$. With the relation $E_{phv} = 4.6 \times 10^{-19}\,\mathrm{Vm}^2 \times c_{Fe^{3+}}$ (derived from [26]) we get $E_D = E_{phv}$ for $c_{Fe^{3+}} = 2.4 \times 10^{24}\,\mathrm{m}^{-3}$. According to (17), the required concentration $c_{Fe^{3+}}$ should also be much larger than this value. With the parameters given above we get $E'_q = 3.4\,\mathrm{MV/m}$. Thus $c_{Fe^{3+}}$ must be also much larger than $7.4 \times 10^{24}\,\mathrm{m}^{-3}$ in order to fulfill assumption (18). A concentration of, for example, $c_{Fe^{3+}} = 20 \times 10^{24}\,\mathrm{m}^{-3}$ fulfills all

requirements (16)–(18). Because the $c_{Fe^{2+}}$ concentration is small (see (16)), the overall iron concentration is in a good approximation equal to $c_{Fe^{3+}}$. Thus the optimum iron concentrations are about 0.06 wt. % Fe_2O_3 or higher.

Only the dynamic range has been taken into consideration in the above optimization analysis. The response time can be decreased at the expense of dynamic range in several ways. An increase of the concentration ratio $c_{Fe^{2+}}/c_{Fe^{3+}}$ enhances the photoconductivity and decreases the response time ($\tau_r \approx \tau_e = \epsilon\epsilon_0/\sigma_{ph}$). The photoconductivity can also be increased by doping with Mg [26], but the dynamic range is lowered in both cases.

1.6 Role of infrared light

The absorption cross section S depends on the light wavelength λ. An increase of λ from 514 nm to 760 nm yields an at least 20 times smaller S [13]. Thus (21) promises that near-infrared light boosts the $M/\#$ to values above 100. The physical origin is evident: A small S enables the presence of many absorbing electrons in the material, which are available for creation of the space-charge field. However, very high doping levels are required (of the order of 0.5 wt. % Fe_2O_3), and it is not sure whether the material parameters are unchanged if the doping level exceeds the optimum for green light (0.06 wt. % Fe_2O_3). Maybe parameters such as the recombination coefficient r change for large iron concentrations. It is highly desired to get information about the properties of heavily doped $LiNbO_3$:Fe.

2 Experimental methods

2.1 Crystals

Several iron-doped $LiNbO_3$ crystals are investigated. They are grown by the Czochralski technique. Relevant crystal parameters are summarized in Table 1. Iron doping is performed by adding the oxide Fe_2O_3 to the melt. It has been checked with atomic-absorption spectroscopy for some of the samples that the distribution coefficient of Fe is one [13], i.e. the Fe concentrations in the melt and in the crystal are the same. The iron concentration c_{Fe} of the samples used in this investigation ranges from $7 \times 10^{24}\,m^{-3}$ to $56 \times 10^{24}\,m^{-3}$ (0.02 to 0.17 wt. % Fe_2O_3). The concentration $c_{Fe^{2+}}$ of filled iron traps (Fe^{2+}) is deduced from absorption measurements [13]. Iron occurs in $LiNbO_3$ in the valence states Fe^{2+} and Fe^{3+}, only. Thus the concentration of empty traps $c_{Fe^{3+}}$ is $c_{Fe^{3+}} = c_{Fe} - c_{Fe^{2+}}$, where c_{Fe} is the total iron content. It cannot be ruled out that the distribution coefficient of iron deviates from one for high iron contents, and neutron activation analysis experiments are on the way to check whether such an effect exists.

Table 1. Notation, dimensions, and total iron concentration c_{Fe} of the investigated $LiNbO_3$ crystals (b: thickness of the crystal; c: length of the polar axis). The first term of the notation refers to the crystal boule, the second part enumerates the pieces that have been prepared

Notation	$a \times b \times c/mm^3$			$c_{Fe}/10^{24}\,m^{-3}$
T02-25-3	3.19	0.85	4.40	7.0
T02-00	3.02	0.85	4.16	7.0
713-2	4.01	1.11	5.01	20.2
713-3	3.99	1.10	5.00	20.2
713-14	3.99	1.12	4.99	20.2
714-20	4.02	0.97	5.13	20.2
750-12	4.03	0.85	5.01	30.3
750-19	3.94	0.32	5.11	30.3
750-22	4.06	0.33	5.14	30.3
751-8	3.94	0.85	5.09	40.4
751-9	3.99	0.85	5.15	40.4
751-12	4.00	0.31	4.94	40.4
751-29	3.99	0.31	5.09	40.4
752-24	4.01	0.29	4.90	50.5
DT2-8	4.67	5.14	5.24	56.0
DT2-17	4.78	1.18	4.92	56.0
DT2-18	4.94	1.17	5.06	56.0

2.2 Holography

A standard two-beam interference setup is utilized (see Fig. 1). Ordinarily polarized light of an argon-ion laser (wavelength 514 nm, green) or of a titanium-sapphire laser (wavelength 760 nm, infrared, IR) is expanded and spatially filtered. A non-polarizing beam-splitter cube divides the light into two beams which are directed onto the crystal in the transmission geometry (spatial frequencies $(2\pi/1.2)\ \mu m^{-1} = 5.2\,\mu m^{-1}$ for green and $(2\pi/1.8)\ \mu m^{-1} = 3.5\,\mu m^{-1}$ for infrared light). The sample is mounted on a motor-driven rotatable stage. The light intensity can be continuously adjusted by a combination of a $\lambda/2$ waveplate and a Glan-laser polarizer. We use light intensities up to $5\,kW\,m^{-2}$ (green) and $40\,kW\,m^{-2}$ (IR). Detectors measure the light intensities behind the crystal. Small apertures in front of the detectors enable their exact adjustment to the center of the beams.

One of the mirrors is piezoelectrically supported to enable active phase stabilization during hologram recording [41, 42]. An alternating voltage ($\omega/2\pi = 984\,s^{-1}$) is applied and a corresponding phase-modulation is created. Beam coupling causes an intensity modulation of the transmitted waves. Amplitudes of first- and second-harmonic signals are detected

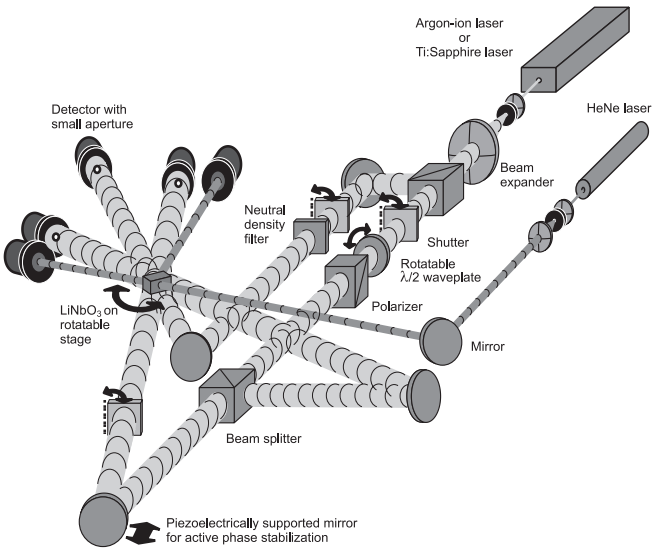

Fig. 1. Schematic diagram of the utilized holographic setup

with the help of two lock-in amplifiers. The second-harmonic amplitude $I^{2\omega}$ is proportional to $\sin\phi$, where ϕ denotes the phase difference between the light intensity pattern $I(z)$ and the refractive-index modulation $\Delta n(z)$. The ϕ is assumed to be 0 or 180° for a properly adjusted interference pattern, and $I^{2\omega}$ can be used as an error signal. The phase of one of the recording beams is shifted to maintain $I^{2\omega} = 0$ all the time. The result is an interference pattern with an actively fixed position with respect to the crystal. Reproducible holographic recording over long times is possible by this technique.

Holograms are written until saturation is reached, and the diffraction efficiency is obtained by blocking one of the writing beams. The remaining beam reads the hologram, and the diffraction efficiency $\eta = I_\mathrm{d}/(I_\mathrm{d} + I_\mathrm{t})$ is determined by measuring the intensities of the diffracted (I_d) and the transmitted light (I_t). The saturation value Δn_s of the refractive-index modulation can be deduced according to Kogelnik's formula $\eta = \sin^2[(\pi\,\Delta n\,d)/(\lambda\cos\Theta)]$ [43], where d is the thickness of the crystal, λ the vacuum light wavelength, and Θ the half-angle between the recording beams inside the crystal. Employment of active stabilization enables incremental recording [44, 45]. Here M holograms of equal diffraction efficiency are superimposed. Angular multiplexing is used and, for readout, the rocking curve $\eta(\vartheta)$ is measured (ϑ denotes the turning angle of the sample). The intensity of the readout light is reduced by a factor of about 100 to avoid erasure of the written holograms. The formula $\Delta n_\mathrm{s} = \Delta n_{\mathrm{s},M} \times M$ [33] yields also the saturation value Δn_s of the refractive-index modulation, where $\Delta n_{\mathrm{s},M}$ is the amplitude of each individual refractive-index grating. The advantage compared to recording of a single hologram into saturation is that breakdowns of the space-charge field are avoided because each hologram is always below the breakdown threshold (10 MV/m) [46]. Furthermore, the active stabilization works only up to $(\pi\,\Delta n\,d)/(\lambda\cos\Theta) = \pi/2$ ($\eta = 1$) even if Δn is not in saturation [47]. Multiplexing of several holograms ensures $\eta < 1$ for all of them. In our experiments, multiplexing of four or ten holograms is carried out.

2.3 Bulk photovoltaic effect

Bulk photovoltaic current densities are measured directly by illuminating the crystals homogeneously with light of a xenon arc lamp which has passed a monochromator system. The intensity I_in of the incident light is measured in front of the crystal – the averaged intensity I in the sample is calculated using the formula $I = I_\mathrm{in}(1-R)(\alpha d)^{-1}[1-\exp(-\alpha d)][1-R\exp(\alpha d)]^{-1}$ (R denotes the reflectivity and α the absorption constant), taking into account absorption and reflection. All intensity values given in the following are calculated with this formula. The surfaces of the samples which are perpendicular to the $\boldsymbol{c}$ axis are contacted with silver paste and connected to a high-sensitive electrometer, which detects the photovoltaic current. A detailed description of this setup can be found in [48].

2.4 Photoconductivity

To investigate the photoconductivity σ_ph, the decay of a holographic grating (fringe spacing $\Lambda = 1.2\,\mu\mathrm{m}$) in presence of erasure light is monitored. An additional beam splitter (see Fig. 1) is inserted to obtain a third light beam which erases a previously written grating. The intensity of this erasure beam can be varied from 0.2 up to 2.5 kW m^{-2} by means of neutral density filters. The diffraction efficiency $\eta(t)$ is observed during the grating decay utilizing a He-Ne laser beam (633 nm, ordinary polarization) which enters the sample under the Bragg angle.

3 Experimental results

3.1 Saturation values of the refractive index changes

Figure 2 shows the obtained saturation values of the refractive-index changes Δn_s, plotted vs. the concentration $c_{\mathrm{Fe}^{3+}}$ of empty traps for several crystals. The saturation amplitude Δn_s grows linearly with the $c_{\mathrm{Fe}^{3+}}$ content in the range of $0 < c_{\mathrm{Fe}^{3+}} < 20\times10^{24}\,\mathrm{m}^{-3}$. We obtain $\Delta n_\mathrm{s}/c_{\mathrm{Fe}^{3+}} = 3.0\times10^{-29}\,\mathrm{m}^3$ (Sommerfeldt et al. [26], $\Delta n_\mathrm{s}/c_{\mathrm{Fe}^{3+}} = 3.4\times10^{-29}\,\mathrm{m}^3$) for green light ($\lambda = 514\,\mathrm{nm}$), and $\Delta n_\mathrm{s}/c_{\mathrm{Fe}^{3+}} = 1.4\times10^{-29}\,\mathrm{m}^3$ for IR light ($\lambda = 760\,\mathrm{nm}$). However, no further increase of Δn_s can be observed for higher concentrations $c_{\mathrm{Fe}^{3+}}$. The maximum values are about 7×10^{-4} for green and 2.8×10^{-4} for IR light. The Δn_s values are independent of K around the spatial frequencies used (see Fig. 3), indicating that saturation of the refractive-index changes for $c_{\mathrm{Fe}^{3+}}$ concentrations above $20\times10^{24}\,\mathrm{m}^{-3}$ (Fig. 2) cannot be attributed to trap limitation. A $1/K$ dependence of Δn_S ((9) and (19)) is not observed, because the Fe^{2+} concentration of the crystals is too large ((18) is not fulfilled).

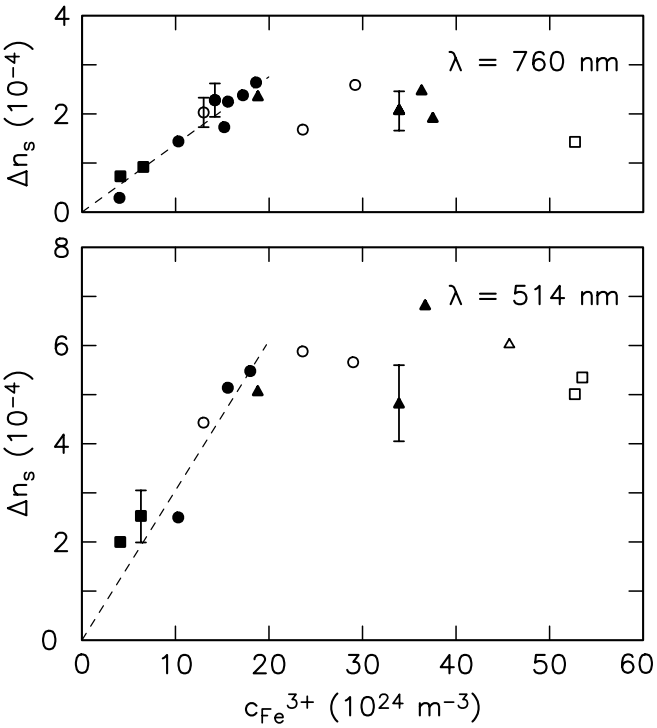

Fig. 2. Saturation values of the refractive-index changes Δn_s vs. trap concentration $c_{\mathrm{Fe}^{3+}}$ measured for green (*bottom*) and IR light (*top*). *Symbols* represent data, and the *dashed lines* are linear fits in the range $0 < c_{\mathrm{Fe}^{3+}} < 20\times10^{24}\,\mathrm{m}^{-3}$

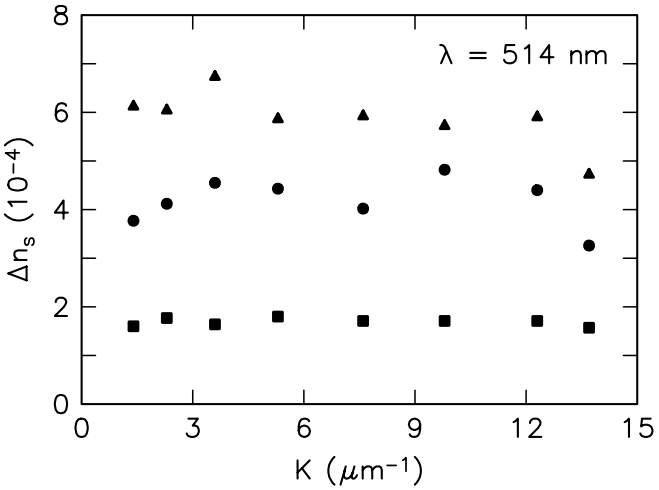

Fig. 3. Saturation values of the refractive-index changes Δn_s vs. spatial frequency K for different samples (*squares*: $c_{Fe^{3+}} = 4.1 \times 10^{24}\,m^{-3}$, $c_{Fe^{2+}} = 2.9 \times 10^{24}\,m^{-3}$, *triangles*: $c_{Fe^{3+}} = 36.7 \times 10^{24}\,m^{-3}$, $c_{Fe^{2+}} = 3.7 \times 10^{24}\,m^{-3}$, *circles*: $c_{Fe^{3+}} = 53.5 \times 10^{24}\,m^{-3}$, $c_{Fe^{2+}} = 2.5 \times 10^{24}\,m^{-3}$)

3.2 Bulk photovoltaic effect

The bulk photovoltaic current is measured for different samples with various concentrations $c_{Fe^{2+}}$ of filled traps at $\lambda = 514\,nm$. The dependence of the bulk photovoltaic current density j_{phv} on the averaged light intensity I in the crystal is shown in Fig. 4a for the sample DT2-17. A linear increase of $j_{phv}(I)$ can be observed. In a next step, the influence of $c_{Fe^{2+}}$ on the ratio j_{phv}/I is investigated. We present in Fig. 4b the obtained results for different samples of the DT2 series. The bulk photovoltaic current density j_{phv}/I depends within the measuring accuracy linearly on the concentration of filled traps $c_{Fe^{2+}}$. Figure 4c shows the dependence of the specific bulk photovoltaic constant $\beta^* = j_{phv}/(I c_{Fe^{2+}})$ on the total amount of iron c_{Fe}. Only a small increase of β^* can be seen for high concentrations of iron in the samples.

3.3 Photoconductivity

The measured photoconductivities σ_{ph} at the wavelength $\lambda = 514\,nm$ are presented in Fig. 5. Plot 5a shows the dependence of σ_{ph} on the light intensity. A linear increase of $\sigma_{ph}(I)$ is obvious. Therefore we look for the relation between the ratio σ_{ph}/I and the concentration ratio $c_{Fe^{2+}}/c_{Fe^{3+}}$. This is shown in Fig. 5b. We obtain $\sigma_{ph}/I \propto c_{Fe^{2+}}/c_{Fe^{3+}}$. Of special interest is the specific photoconductivity $(\sigma_{ph}/I)/(c_{Fe^{2+}}/c_{Fe^{3+}})$. Figure 5c shows this specific photoconductivity as a function of the total iron concentration c_{Fe} of the samples. These measurements reveal a remarkable result: A strong increase of $(\sigma_{ph}/I)/(c_{Fe^{2+}}/c_{Fe^{3+}})$ is observed for iron concentrations c_{Fe} exceeding $20 \times 10^{24}\,m^{-3}$.

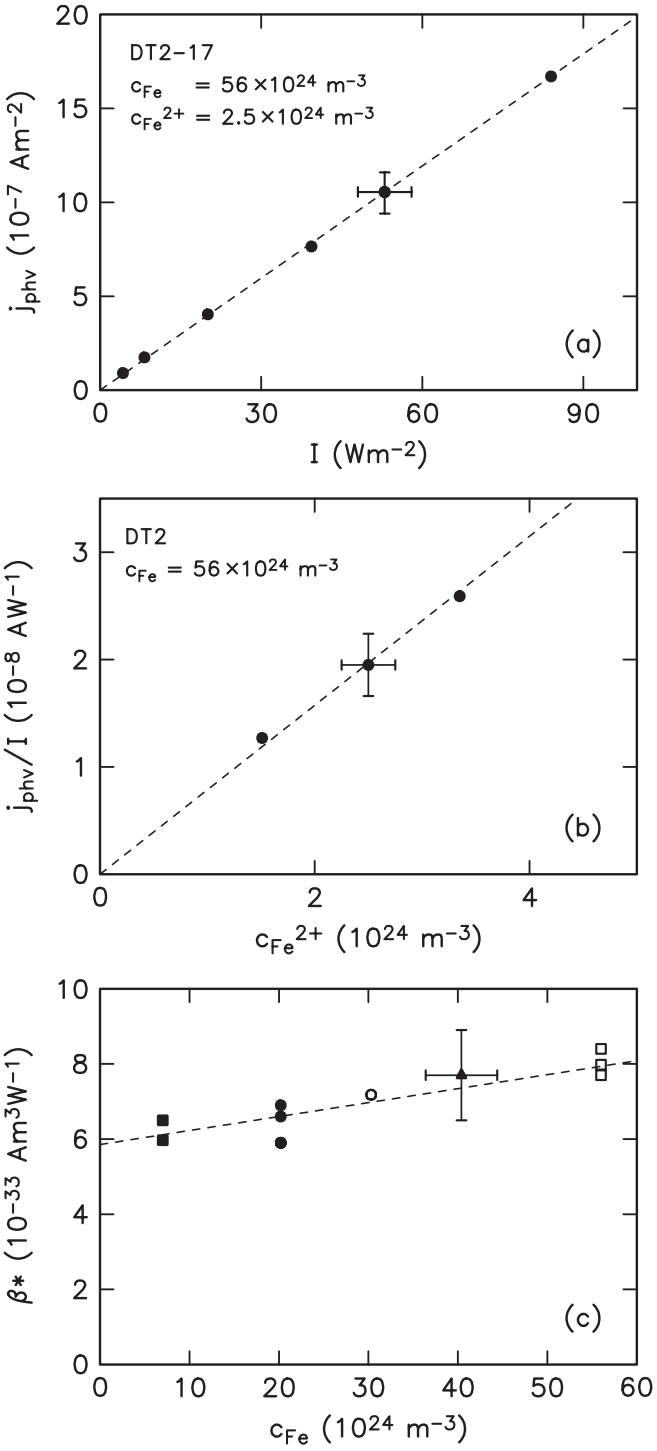

Fig. 4a–c. Measured data (*symbols*) and linear fits (*dashed lines*). **a** Bulk photovoltaic current density j_{phv} vs. light intensity I for $\lambda = 514\,nm$, measured in sample DT2-17. **b** Ratio j_{phv}/I vs. concentration $c_{Fe^{2+}}$ of filled traps for crystals of boule DT2. **c** Specific photovoltaic coefficient $\beta^* = (j_{phv}/I)/c_{Fe^{2+}}$ vs. total iron concentration c_{Fe}

4 Discussion

4.1 Saturation values of the refractive-index changes

The measurements reveal that the relations (10)–(12) are valid only for iron concentrations c_{Fe} smaller than $20 \times 10^{24}\,m^{-3}$ (0.06 wt. % Fe_2O_3). The ratios $\Delta n/c_{Fe^{3+}}$, $j_{phv}/(I\,c_{Fe^{2+}})$, and $(\sigma_{ph}/I)/(c_{Fe^{2+}}/c_{Fe^{3+}})$ depend on the overall iron concentration c_{Fe}. The influence of c_{Fe} on the normalized photovoltaic current density is weak, but the normalized photoconductivity $(\sigma_{ph}/I)/(c_{Fe^{2+}}/c_{Fe^{3+}})$ increases almost by a factor of 5 in the investigated c_{Fe} range. One or several of the following pa-

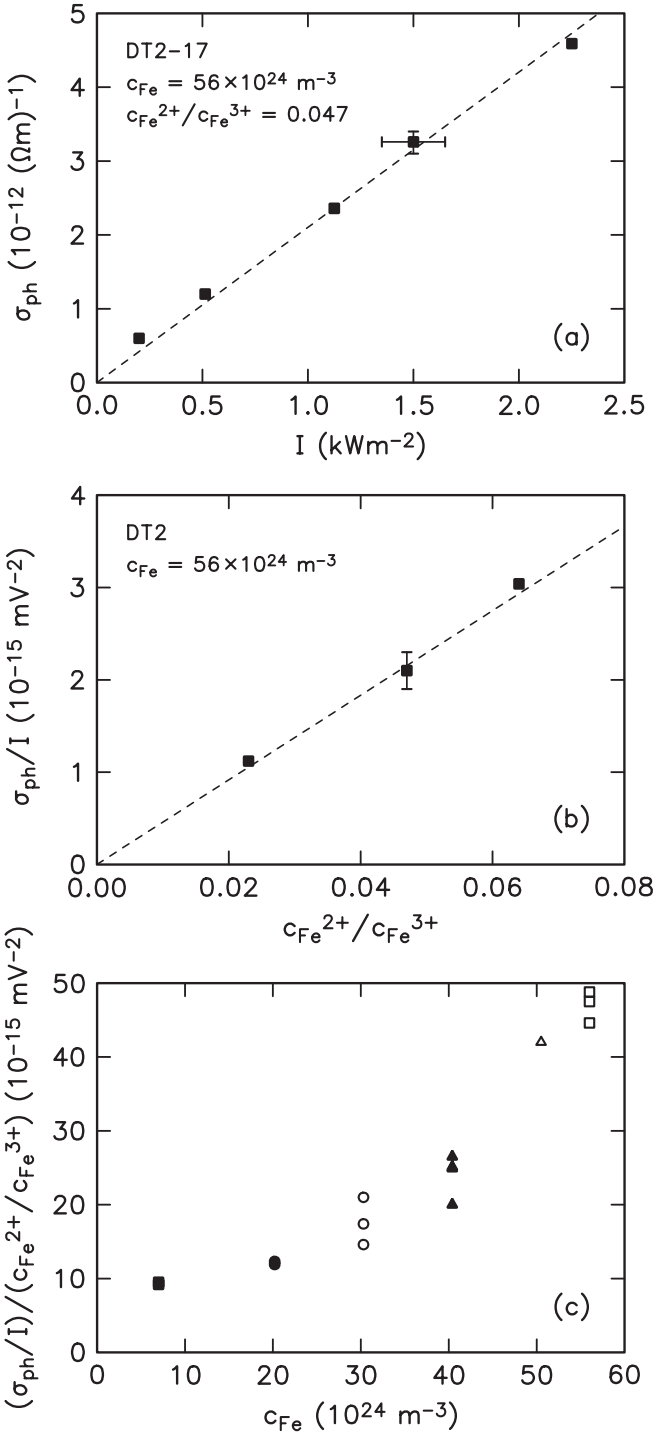

Fig. 5a–c. Measured data (*symbols*) and linear fits (*dashed lines*). **a** Photoconductivity σ_{ph} vs. light intensity I (sample DT2-17). **b** Ratio σ_{ph}/I vs. $c_{Fe^{2+}}/c_{Fe^{3+}}$ for crystals of boule DT2. **c** Specific photoconductivity $(\sigma_{ph}/I)/(c_{Fe^{2+}}/c_{Fe^{3+}})$ vs. total iron concentration c_{Fe}

rameters depend on the iron concentration: q, S, r, μ. Further experiments are required to elucidate the origin of the increase of the photoconductivity. Maybe iron ions occupy different lattice sites depending on the doping level or pairs of associated iron centres are created. Investigations with other dopants, for example copper, may reveal whether the doping concentration 20×10^{24} m^{-3} is a general threshold value. Maybe higher copper concentrations are acceptable without boosting the conductivity. It is also worth varying in further experiments the Li/Nb concentration ratio. This may influence the lattice position of iron. Large Li deficits can also decrease further charge carrier mobility and conductivity, because Li vacancies impede movement of conduction band electrons. Furthermore, the impact of higher harmonics on the processes deserves special attention, because light patterns with modulation degrees close to unity are employed in both experiments and applications.

4.2 Achieved dynamic ranges

State of the art are refractive-index changes of 7×10^{-4} for green and 2.8×10^{-4} for near-infrared light. Equations (14) and (15) yield the $M/\# = 11$ for green and 5 for near-infrared light (once more assuming $\tau_e \approx \tau_r$). Crystals with about 0.06 wt. % Fe_2O_3 are necessary to achieve these values. Infrared light provides no advantage regarding the dynamic range so far. Larger doping levels are required to benefit from the smaller absorption cross section S of infrared light, but the dramatic increase of the photoconductivity makes the highly doped material unattractive.

4.3 Recording with infrared light

Anyhow, it is worth noting that holograms can be recorded in iron-doped $LiNbO_3$ with continuous wave light of 760 nm wavelength, and an $M/\#$ of 5 is acceptable for several applications. The refractive-index changes for infrared light are about 2.5 times smaller than those for green light. Taking into consideration the wavelength dependence of the refractive index [36] and of the electro-optic coefficient [38], it turns out that the space-charge field is about 2.1 times reduced for infrared light compared with recording by green illumination (see (9)). Obviously, a shift of the recording wavelength from the visible to the infrared has detrimental influence on the ratio of photovoltaic current density and photoconductivity (see (6)). A further remarkable difference for recording with visible and infrared light is the response time $\tau_r = \tau_e = \epsilon\epsilon_0/\sigma_{ph}$. Just changing the wavelength, and keeping the concentration ratio $c_{Fe^{2+}}/c_{Fe^{3+}}$ and the light intensity constant, the response time is about 100 times larger for infrared than for green light. Anyhow, this can be compensated by further reduction of the material (increase of $c_{Fe^{2+}}/c_{Fe^{3+}}$) and by use of higher light intensities. Low absorption makes it possible to use high infrared light powers without running into trouble with heating of the material. Furthermore, the small absorption of infrared light is advantageous for the homogeneity of thick holograms.

5 Summary

The major outcomes of the present investigation are as follows:

– Theoretical considerations reveal that the photon absorption cross section S of dopants is a crucial parameter for limitation of the dynamic range of photorefractive materials. Small S enable the presence of many electrons which can be used for creation of the space-charge field without causing huge absorption.

– The measured light-induced refractive-index changes in $LiNbO_3$ increase linearly with the Fe^{3+} concentration up to $20 \times 10^{24}\,m^{-3}$ (corresponds to 0.06 wt. % Fe_2O_3 for small Fe^{2+} contents) and saturate for larger Fe^{3+} concentrations.
– The best performance of $LiNbO_3$:Fe with respect to the dynamic range and the multiplexing capability can be expected with crystals of an iron concentration of $20 \times 10^{24}\,m^{-3}$ (0.06 wt. % Fe_2O_3). The optimum absorption is $\alpha = 2/d$, where d is the thickness of the material.
– Recording with infrared light (wavelength 760 nm) in $LiNbO_3$:Fe is possible. Refractive-index changes are about 2.5 times smaller and response times are about 100 times larger than for green light under otherwise unchanged experimental conditions. Anyhow, good availability of infrared light sources and low absorption of infrared light may compensate for these drawbacks.

Acknowledgements. Fruitful and enlightening discussions with E. Krätzig are highly appreciated. Financial support by the Deutsche Forschungsgemeinschaft (SFB 225, C5) is gratefully acknowledged.

References

1. A. Ashkin, G.D. Boyd, J.M. Dziedzic, R.G. Smith, A.A. Ballman, J.J. Levinstein, K. Nassau: Appl. Phys. Lett. **9**, 72 (1966)
2. F.S. Chen, J.T. LaMacchia, D.B. Fraser: Appl. Phys. Lett. **13**, 223 (1968)
3. F.H. Mok: Opt. Lett. **18**, 915 (1993)
4. D. Psaltis, F. Mok: Sci. Am. **273**(5), 70 (November 1995)
5. I. McMichael, W. Christian, D. Pletcher, T.Y. Chang, J.H. Hong: Appl. Opt. **35**, 2375 (1996)
6. D. Lande, S.S. Orlov, A. Akella, L. Hesselink, R.R. Neurgaonkar: Opt. Lett. **22**, 1722 (1997)
7. V. Leyva, G.A. Rakuljic, B. O'Conner: Appl. Phys. Lett. **65**, 1079 (1994)
8. R. Müller, M.T. Santos, L. Arizmendi, J.M. Cabrera: J. Phys. D: Appl. Phys. **27**, 241 (1994)
9. S. Breer, K. Buse: Appl. Phys. B **66**, 339 (1998)
10. G.E. Peterson, A.M. Glass, T.J. Negran: Appl. Phys. Lett. **19**, 130 (1971)
11. J.J. Amodei, W. Phillips, D.L. Staebler: Appl. Opt. **11**, 390 (1972)
12. A.M. Glass, D. von der Linde, T.J. Negran: Appl. Phys. Lett. **25**, 233 (1974)
13. H. Kurz, E. Krätzig, W. Keune, H. Engelmann, U. Gonser, B. Dischler, A. Räuber: Appl. Phys. **12**, 355 (1977)
14. R.R. Shah, D.M. Kim, T.A. Rabson, F.K. Tittel: J. Appl. Phys. **47**, 5421 (1976)
15. E. Krätzig, R. Orlowski: Opt. Quantum Electron. **12**, 495 (1980)
16. E. Krätzig, R. Orlowski: Ferroelectrics **27**, 241 (1980)
17. E. Krätzig: Ferroelectrics **21**, 635 (1978)
18. E. Krätzig, R. Orlowski, V. Doormann, M. Rosenkranz: SPIE **164**, 33 (1978)
19. E. Krätzig, H. Kurz: Opt. Acta **24**, 475 (1977)
20. R. Orlowski, E. Krätzig: Solid State Commun. **27**, 1351 (1978)
21. D.L. Staebler, J.J. Amodei: J. Appl. Phys. **43**, 1042 (1972)
22. G.A. Brost, R.A. Motes, J.R. Rotgé: J. Opt. Soc. Am. B **5**, 1879 (1988)
23. K. Buse, E. Krätzig: Appl. Phys. B **61**, 27 (1995)
24. F. Jermann, J. Otten: J. Opt. Soc. Am. B **10**, 2085 (1993)
25. K. Buse, S. Loheide, D. Sabbert, E. Krätzig: J. Opt. Soc. Am. B **13**, 2644 (1996)
26. R. Sommerfeldt, L. Holtmann, E. Krätzig, B.C. Grabmaier: Phys. Status Solidi A **106**, 89 (1988)
27. E. Krätzig, H. Kurz: J. Electrochem. Soc. **124**, 131 (1977)
28. H. Kurz: Philips Tech. Rev. **37**, 109 (1977)
29. R.A. Rupp, R. Sommerfeldt, K.H. Ringhofer, E. Krätzig: Appl. Phys. B **51**, 364 (1990)
30. K. Buse: Appl. Phys. B **64**, 273 (1997)
31. N.V. Kukhtarev, V.B. Markov, S.G. Odoulov, M.S. Soskin, V.L. Vinetskii: Ferroelectrics **22**, 949, 961 (1979)
32. R. Magnusson, T.K. Gaylord: Appl. Opt. **13**, 1545 (1974)
33. F.H. Mok, G.W. Burr, D. Psaltis: Opt. Lett. **21**, 896 (1996)
34. N.V. Kukhtarev: Sov. Tech. Phys. Lett. **2**, 438 (1976)
35. J.M.C. Jonathan, R.W. Hellwarth, G. Roosen: IEEE J. Quant. Electron. **QE-22**, 1936 (1986)
36. D.F. Nelson, R.M. Mikulyak: J. Appl. Phys. **45**, 3688 (1974)
37. K. Onuki, N. Uchida, T. Saku: J. Opt. Soc. Am. **62**, 1030 (1972)
38. S. Fries, S. Bauschulte: Phys. Status Solidi A **125**, 369 (1991)
39. R.T. Smith, F.S. Welsh: J. Appl. Phys. **42**, 2219 (1971)
40. A. Mansingh, A. Dhar: J. Phys. D: Appl. Phys. **18**, 2059 (1985)
41. P.A.M. Dos Santos, L. Cescato, J. Frejlich: Opt. Lett. **13**, 1014 (1988)
42. S. Breer, K. Buse, K. Peithmann, H. Vogt, E. Krätzig: Rev. Sci. Instrum. **69**, 1591 (1998)
43. H. Kogelnik: Bell Syst. Tech. J. **48**, 2909 (1969)
44. Y. Taketomi, J.E. Ford, H. Sasaki, J. Ma, Y. Fainman, S.H. Lee: Opt. Lett. **16**, 1774 (1991)
45. K. Peithmann, K. Buse, A. Wiebrock, E. Krätzig: Opt. Lett. **23**, 1927 (1998)
46. K. Buse, S. Breer, K. Peithmann, S. Kapphan, M. Gao, E. Krätzig: Phys. Rev. B **56**, 1225 (1997)
47. V.P. Kamenov, K.H. Ringhofer, B.I. Sturman, J. Frejlich: Phys. Rev. A **56**, R2541 (1997)
48. K. Buse, U. van Stevendaal, R. Pankrath, E. Krätzig: J. Opt. Soc. Am. B **13**, 1461 (1996)